

Topology optimization using a continuous density field and adaptive mesh refinement

Andrew B. Lambe¹  | Aleksander Czekanski²

¹Department of Mathematics and Industrial Engineering, École Polytechnique de Montréal, Montreal, H3T 1J4, Canada

²Department of Mechanical Engineering, Lassonde School of Engineering, York University, Toronto, M3J 1P3, Canada

Correspondence

Andrew B. Lambe, Department of Mathematics and Industrial Engineering, École Polytechnique de Montréal, Montreal H3T 1J4, Canada.
Email: andrew.lambe@polymtl.ca

Summary

A new method of topology optimization is introduced in which a continuous material field is combined with adaptive mesh refinement. Using a continuous material field with different analysis and design meshes allows the method to produce optimal designs that are free of numerical artifacts like checkerboard patterns and material islands. Adaptive mesh refinement is then applied to both meshes to precisely locate the optimal boundary of the final structure. A Helmholtz-type density filter is used to prevent the appearance of small topological features as the mesh refinement proceeds. Results are presented for several test problems, including problems with geometrically complex domain boundaries.

KEY WORDS

optimization, topology design, finite element methods, adaptivity, elasticity, continuous material

1 | INTRODUCTION

In topology optimization, the optimal distribution of material in a given domain to accomplish a given task is sought. Topology optimization problems arise in a range of applications such as solid mechanics, fluid mechanics, heat transfer, acoustics, and electromagnetics.¹ In structural design, the problem is often formulated as a minimum compliance or maximum stiffness problem subject to a constraint on the fraction of the design domain that is filled with material. The most common way to parametrize the design domain is the density-based approach.¹ In its most basic form, the density approach divides the design domain into elements and assigns each element a density design variable representing the fraction of that element containing solid material. Penalization is applied to intermediate density values to force the optimal design to consist mainly of solid and void elements. While this setup does not guarantee that all elements will be either solid or void at the optimal design, it does permit the use of fast gradient-based optimization algorithms to solve the problem.

The main challenges with using element-based design variables are the mesh-dependency of the optimal topology and the possible appearance of “checkerboard” patterns of solid and void elements. A variety of techniques has been developed to mitigate these issues. Density filters² select the element density used in the analysis as the weighted average of a set of design variables in the neighborhood of that element. Sensitivity filters³ modify the gradients using a similar weighted average approach to avoid converging on a checkerboard design. Both filters can be efficiently implemented as the solution of a Helmholtz differential equation over the design domain.⁴ Because filtering generally produces a transition region between solid and void parts of the optimal topology, a nonlinear projection method⁵ can be applied to reduce the size of this region. The filter and projection methods also possess the ability to control the minimum size of the features present in the optimal topology, even when very fine meshes are used.

Other approaches to producing checkerboard-free topologies come from alternative parametrizations of the design space. For example, in their projection scheme, Guest et al⁵ assign design variables to the nodes of the mesh, rather than the elements themselves. Matsui and Terada⁶ define the design variables as scaling coefficients of first-order finite element shape functions so that the density field becomes continuous. Nguyen et al⁷ use multiple design variables in each analysis element to produce a fine-resolution estimate of the optimal topology on a coarse analysis mesh. Many recent approaches advocate decoupling the design variable mesh from the structural analysis mesh. Kang and Wang⁸ assign design variables to points in the design domain and use Shepard interpolation to compute the density at a given point. Qian⁹ takes the design variables to be scaling coefficients of B-spline basis functions, providing a smooth estimate of the optimal density field. Paulino and Le¹⁰ note that the checkerboard phenomenon can be alleviated by constraining the gradient of the density field in the parametrization. All of these alternative parametrizations implicitly constrain the gradient through either averaging of nearby design variables or imposing continuity on the density field itself.

Unfortunately, these alternative parametrizations suffer from the same issue as filtering the element-based variables: They explicitly create a transition region along the boundary of the structure. In applications where explicit knowledge of the boundary is required, this is a serious drawback of density-based topology optimization methods compared with level-set methods.¹¹ While nonlinear projection may be used to sharpen the boundary, projection functions like the smoothed Heaviside function require careful selection of a smoothing parameter¹² to balance the sharpness of the boundary with the difficulty of solving the modified optimization problem.

In cases where the density field is represented by a continuous function, the size of the transition region is driven by the mesh size. Therefore, mesh refinement may be used as an alternative to nonlinear projection. Refinement has been used in conjunction with topology optimization before, though mainly with element-based design variables.^{13–16} Guest and Smith Genut¹⁷ applied adaptive coarsening and refinement strictly to the design variable mesh. Wang et al¹⁸ adaptively refine both the design and analysis meshes using different refinement indicators for each mesh.

In this work, we combine a continuous density field parametrized by finite element shape functions (following Matsui and Terada⁶) with an adaptive mesh refinement scheme to sharpen our estimate of the structural boundary. We use our initial mesh to define the minimum feature size we desire in the optimal topology, rather than a filter. While these initial large features are not lost with adaptive mesh refinement, our previous work¹⁹ indicated that small holes and structural members could emerge in places where the mesh is refined. Therefore, we use the Helmholtz density filter⁴ with a small radius to prevent such features from emerging as the mesh refinement proceeds. The resulting topology optimization method uses tools from the finite element method for both analysis and design parametrization and can be applied easily to geometrically complex domains.

The remainder of this paper is organized as follows. Section 2 describes the parametrization of the density field. Section 3 describes the adaptive mesh refinement scheme as well as the mesh refinement indicator. Section 4 reviews the Helmholtz density filter and its application in the presented method. Section 5 shows our results on 4 different two-dimensional test problems.

2 | DESIGN SPACE PARAMETRIZATION

We consider the problem of minimizing the compliance (ie, maximizing the stiffness) of a linearly elastic structure subject to a constraint on the volume of solid material in the design domain. Formally, the optimization problem is given by

$$\begin{aligned}
 & \text{minimize} \quad C(\rho) = \frac{1}{2} \mathbf{u}^T \mathbf{K}(\rho) \mathbf{u} \\
 & \text{w.r.t.} \quad \rho \\
 & \text{s.t.} \quad V(\rho) \leq V^* \\
 & \quad 0 \leq \rho \leq 1 \\
 & \text{where} \quad \mathbf{K}(\rho) \mathbf{u} = \mathbf{f},
 \end{aligned} \tag{1}$$

where ρ are the design variables; \mathbf{K} , \mathbf{u} , and \mathbf{f} are the stiffness matrix, displacement vector, and force vector resulting from the finite element discretization of the problem; and $C(\rho)$ and $V(\rho)$ are the compliance and material volume functions, respectively.

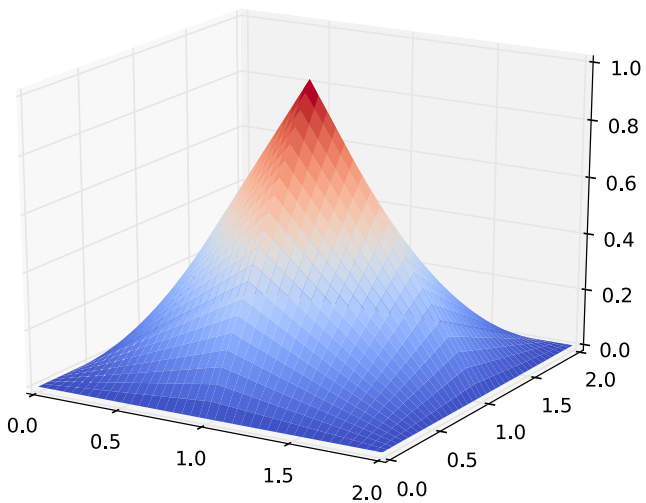


FIGURE 1 A bilinear shape function at the intersection of 4 square finite elements

In this work, we describe material density as a continuous field over the design domain parametrized by linear shape functions. Figure 1 shows a bilinear shape function at the intersection of 4 square elements for a two-dimensional design problem. The vector of design variables ρ then becomes the vector of scaling coefficients for the shape functions. For a two-dimensional design domain Ω , the density field is defined by

$$\rho(x, y) = \sum_{i=1}^{N_d} N_i(x, y) \rho_i. \quad (2)$$

Because the shape functions are nonnegative and sum to one on every element, the bound constraints imposed on ρ in problem (1) are sufficient to ensure $0 \leq \rho(x, y) \leq 1$ everywhere in Ω . Note that the summation in Equation 2 is over the degrees of freedom (DOFs) of the design mesh, which does not need to be the same as the analysis mesh. As a result, the material volume function is defined by the integral

$$V(\rho) = \int_{\Omega} \rho(x, y) d\Omega, \quad (3)$$

and can be evaluated independent of the structural analysis.

Using different meshes for the design parametrization and structural analysis is important to prevent numerical artifacts in the optimized design. As noted in Section 1, using a continuous density field eliminates the possibility of material checkerboard patterns, a phenomenon resulting from using element-based design variables. However, while Matsui and Terada⁶ did not observe any other numerical artifacts in their optimized designs, Rahmatalla and Swan²⁰ noted the appearance of material “islands” not connected to the rest of the structure. The cause of this phenomenon is not clear, though Rahmatalla and Swan note that it can be mitigated by using finer meshes.²⁰ In their tests, they use the same mesh to both parametrize the density field and analyze the structure. Jog and Haber²¹ used a variational analysis to argue that such a configuration could possess numerical instabilities and recommended using higher-order elements in the analysis as a cure. We adopted a slightly different approach in which the element orders are the same but the meshes are different. Specifically, the analysis mesh is a global refinement of the design mesh. This approach increases the number of DOFs in the analysis by the same amount as using second-order elements but is slightly more computationally efficient. (Lower-order finite elements share fewer DOFs with adjacent elements so the resulting linear system is more sparse and easier to solve.) Our test results in Section 5 do not show any “islanding” occurring in our optimized designs.

To assemble the stiffness matrix, we assume that the structure is linearly elastic and penalize intermediate density values using the SIMP (Solid Isotropic Material Penalization) method.²² For a given density value $\rho \in [0, 1]$, the Young modulus of the softened material becomes

$$E(\rho) = E_{min} + \rho^p(E_0 - E_{min}), \quad (4)$$

where $p \geq 1$ and E_{min} is a minimum value to prevent the assembled stiffness matrix from becoming singular. Density and Young modulus values at the quadrature points are determined by evaluating the functions (2) and (4) directly.

3 | ADAPTIVE MESH REFINEMENT

In topology optimization, adaptive coarsening and refinement of the mesh serves multiple purposes. In the analysis of the structure, it can be used to reduce error in the estimated behavior, ie, compliance, stress, and strain. In the design mesh, refinement increases the resolution of the material distribution and can be used to provide a more precise estimate of the structural boundary. Finally, local refinement reduces the computational cost of both the analysis and the optimization by placing fewer DOFs and fewer design variables in large void regions or large regions of solid material. In this work, we are mainly focused on accurately locating the material boundary of the optimum topology.

The continuity of the material field permits a simple definition of the refinement indicator. Any cell of the design mesh that is not dominated by solid or void material likely contains the boundary and should be refined. Thus, we formulate the refinement indicator

$$\eta_e = \left(1 - \frac{\int_{\Omega_e} \rho(x, y) d\Omega_e}{|\Omega_e|} \right) \frac{\int_{\Omega_e} \rho(x, y) d\Omega_e}{|\Omega_e|}, \quad (5)$$

for some element Ω_e . By construction, $0 \leq \eta_e \leq 0.25$ with smaller values indicating that the element is dominated by solid material or a void region. We choose the threshold $\eta_e \geq 0.05$ to indicate that the cell should be refined and $\eta_e \leq 0.01$ to indicate that the cell should be coarsened. In practice, we have found that setting a lower threshold for refinement is more effective because it is more likely to simultaneously refine cells all along the apparent edge of the structure.

We note that Wang et al¹⁸ formulate a similar indicator in their work to refine their design mesh. They use

$$\eta_e = \frac{\int_{\Omega_e} \rho(x, y) d\Omega_e}{|\Omega_e|}, \quad (6)$$

so that $0 \leq \eta_e \leq 1$ and state both upper and lower thresholds on η_e to indicate which candidate cells should be refined or coarsened. The other major difference between our mesh refinement scheme and that of Wang et al is that we do not use a separate refinement indicator for the analysis mesh. In our implementation, the design and analysis meshes are coupled together; the analysis mesh is always derived from the design mesh by refining all cells at least once. Any local refinement or coarsening of the design mesh results in a local refinement or coarsening of the corresponding cells of the analysis mesh.

Once all of the candidate cells have been identified by the indicator (5), local coarsening and refinement take place. However, because the refinement is local, the resulting mesh contains refined cells that are adjacent to unrefined cells. This creates some nodes that do not belong to all adjacent cells, known as “hanging nodes.” Figure 2 shows a simple quadrilateral mesh after one local refinement. The hanging nodes are located at the T-junctions in the mesh. These nodes are problematic because it is easy to choose values for these DOFs to break the continuity of the interpolated function. Therefore, the values of the scaling coefficients at these nodes are constrained so that the function remains continuous. For the case of two-dimensional linear shape functions, the constrained value is just the average of the 2 adjacent DOFs on the coarse cell.

In the structural analysis, these hanging node constraints are imposed implicitly in the optimization problem by modifying the \mathbf{u} values at the hanging nodes so that the corresponding displacement field is continuous. In the density field parameterization, the coefficients ρ are chosen explicitly by the optimizer so we add the hanging node constraints to the optimization problem. As a result, only the optimal density field is guaranteed to be continuous. (In practice, these hanging node constraints are linear equations and are generally easy to satisfy after a few iterations of the optimization algorithm.) The 2 sets of hanging node constraints are updated after every mesh refinement. Our finite element solver, deal.II,²³ contains functions to automatically identify and track the hanging node constraints on given meshes.

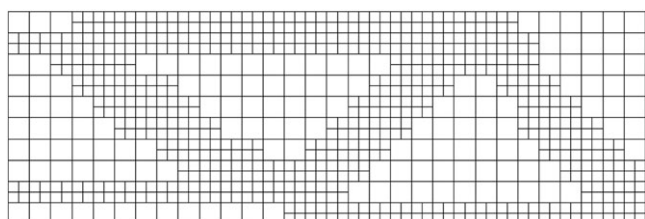


FIGURE 2 A simple quadrilateral mesh after one local refinement. The hanging nodes of the mesh are located at the T-junctions in the figure

To summarize, the following sequence of steps describes our procedure for combining topology optimization and adaptive mesh refinement:

1. Create the initial design mesh and derive the initial analysis mesh via global refinement. Both meshes are populated with first-order finite elements. Choose the initial design to be a uniform density of 0.5.
2. Optimize the topology for the current design and analysis meshes.
3. Calculate the indicator function (5) for each cell in the design mesh.
4. Flag design mesh cells for coarsening if $\eta_e \leq 0.01$. Flag design mesh cells for refinement if $\eta_e \geq 0.05$.
5. Pass the coarsening and refinement flags to the corresponding cells in the analysis mesh. This keeps the analysis mesh more refined than the design mesh to prevent “island” artifacts from appearing.
6. Refine both meshes.
7. If enough mesh refinements have been performed, stop. Otherwise, return to step 2 using the current solution as the starting point of the next optimization.

4 | DENSITY FILTER

As mentioned in our previous work,¹⁹ the method described thus far does not preserve a minimum feature size as the mesh is refined. To prevent the emergence of small topological features, we add a density filter to our scheme.

Basic density filters transform an input density ρ_i into an output density $\bar{\rho}_i$ using a weighted average of density values in the neighborhood of element i . Lazarov and Sigmund⁴ noted that this filter structure is mathematically equivalent to taking $\bar{\rho}$ as the solution of the Helmholtz partial differential equation

$$-r^2 \nabla^2 \bar{\rho} + \bar{\rho} = \rho, \quad (7)$$

where r is the size of the neighborhood. The chief advantage of this interpretation is that Equation 7 can be solved using the same finite element solver already in place for the structural analysis problem on the same mesh. No information about the neighborhood of a given point or element is needed beyond mesh connectivity.

Discretizing Equation 7 using the finite element method results in the linear system of equations

$$\mathbf{K}_H \bar{\rho} = \mathbf{T} \rho, \quad (8)$$

where \mathbf{T} incorporates the mapping of ρ from the design mesh to the analysis mesh. Therefore, \mathbf{T} is a rectangular matrix. The entries of \mathbf{T} are computed by

$$T_{ij} = \int_{\Omega_e} \bar{N}_i(x, y) N_j(x, y) d\Omega_e, \quad (9)$$

where Ω_e is an element of the analysis mesh, N_j is the j th shape function of the unfiltered density field, and \bar{N}_i is the i th shape function of the filtered density field. Critically, the shape functions need not be of the same order. In fact, we have found that interpolating the filtered field using second-order elements, in contrast to the first-order elements in the unfiltered field, helps to keep the filtered density field between 0 and 1 over the entire domain. Finally, note that \mathbf{K}_H and \mathbf{T} are independent of the optimization variables, so they may be formed once for each mesh refinement and reused throughout the optimization procedure to transfer design mesh density information to the analysis mesh.

The filter radius r is generally chosen to be the minimum feature size in the optimum topology. However, our approach uses the initial coarse mesh to control feature size while the filter is used to prevent the emergence of new features in the refined parts of the mesh. Therefore, unlike other density filter implementations in the literature, we set the filter radius to be smaller than the initial mesh size. We can even set the filter radius to be 0. While $r = 0$ would cause $\bar{\rho} = \rho$ in the sense of Equation 7, this does not occur in Equation 8 because

$$K_{H,ij} = \int_{\Omega_e} r^2 [\nabla \bar{N}_i(x, y)]^T \nabla \bar{N}_j(x, y) + \bar{N}_i(x, y) \bar{N}_j(x, y) d\Omega_e, \quad (10)$$

as a result of the finite element discretization. Even if $r = 0$, the fact that \bar{N}_i and \bar{N}_j are not orthogonal causes $K_{H,ij}$ to be nonzero for many values of i and j for which $i \neq j$. Therefore, the discretization has its own (slight) filtering effect; it is not

a strict interpolation from a coarse mesh to a fine one. As we will see in some of the results, this feature is advantageous because we may use adaptive mesh refinement to systematically eliminate the transition region even in the presence of the filter.

While the optimal unfiltered density field is continuous because the corresponding hanging node constraints are enforced through the action of the optimizer, the same cannot be said of the filtered density field. Therefore, to incorporate the filter fully into our method, we need to create an additional set of hanging node constraints for the filtered density field, which is defined on the analysis mesh. This causes the filtered density field to be continuous throughout the optimization even though the unfiltered field may be discontinuous for some iterations. The final set of filtered densities is given by

$$\bar{\rho} = \mathbf{C}_H \mathbf{K}_H^{-1} \mathbf{T} \rho, \quad (11)$$

where \mathbf{C}_H represents the influence of the analysis mesh hanging node constraints. For an unconstrained DOF i , $C_{H,ii} = 1$ and all other row entries are 0. For a constrained DOF i , $C_{H,ii} = 0$ and the other row entries are exactly the coefficients of the hanging node constraint.

5 | RESULTS AND DISCUSSION

Finite element analysis and the parametrization of the design domain were developed using the deal.II library.²³ Deal.II provides objects for applying the finite element method to solve PDEs on arbitrary domains. Of particular relevance to this study, deal.II provides tools for error indicator definition and adaptive mesh refinement to implement the methods described in Section 3. For the first example problem that follows, the meshes were generated directly in deal.II. For the other examples, the meshes were generated using the Gmsh tool.²⁴

The optimization problems were solved using the interior-point solver IPOPT.²⁵ Default settings were used with the following exceptions: The optimality convergence tolerance was set at 10^{-5} , an L-BFGS approximate Hessian was used with 30 pairs of vectors, and an iteration limit of 500 was enforced. These settings improved the convergence of problems with thousands of design variables. Gradient information was computed analytically and passed directly to IPOPT.

The same set of material properties is used in all examples. We set $E_0 = 71$ GPa, $E_{min} = 10^{-9} E_0$, $\nu = 0.33$, and SIMP parameter $p = 3$. The Young modulus and Poission ration are taken from Holmberg et al²⁶ as representative of an aluminum alloy. Finally, the volume fraction limit V^* is set to 0.3, or 30% of the original design domain volume.

5.1 | Messerschmidt-Bolkow-Blohm beam problem

The first example is the classical MBB (Messerschmidt-Bolkow-Blohm) beam problem. Figure 3 depicts the problem geometry. In this example, $F = 150$ N and $L = 100$ mm. Table 1 shows the optimized topologies using 4 different filter radii and 4 levels of refinement from an initial design mesh of 10×30 elements and an initial analysis mesh of 20×60 elements. In all figures, red denotes solid material while blue denotes void. The optimal compliance values are also included for reference.

In our scheme, we use the filter to suppress the appearance of small structural features that may be created in locally refined parts of the mesh. The filter radii presented in Table 1 correspond to one-half, one-quarter, and one-eighth the

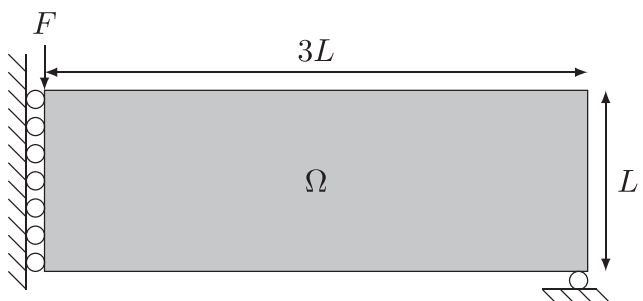
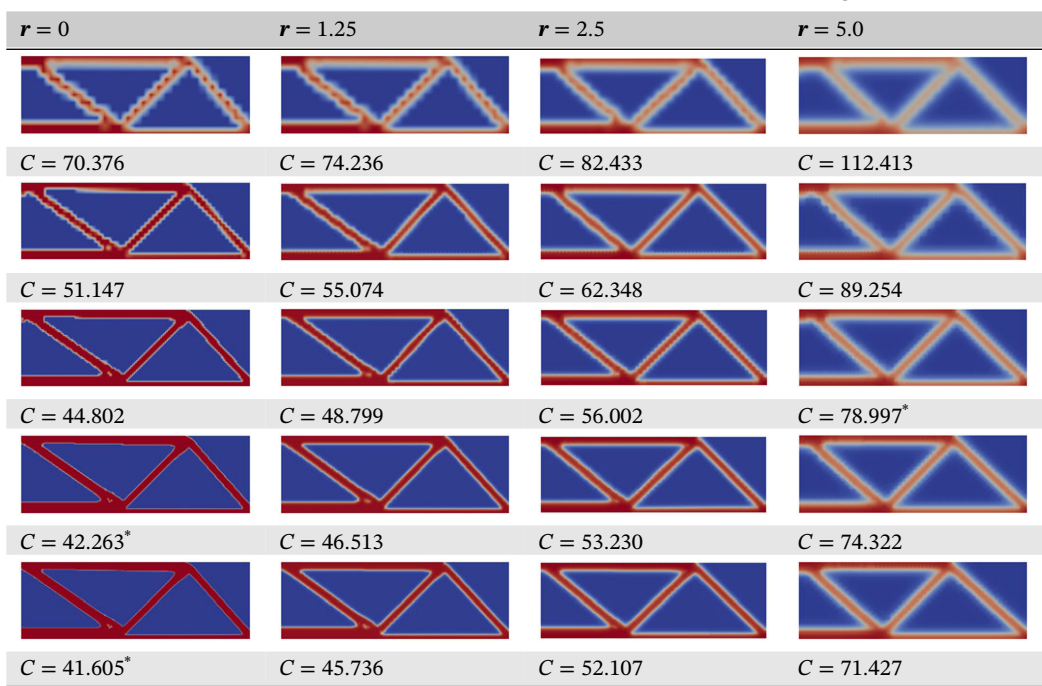


FIGURE 3 The Messerschmidt-Bolkow-Blohm beam problem geometry

TABLE 1 Messerschmidt-Bolkow-Blohm beam example with 10×30 element starting mesh

Note. Compliance values are in N-mm. Results are ordered top-to-bottom, coarsest design mesh to finest.

*This indicates that the desired optimality tolerance could not be achieved for that problem.

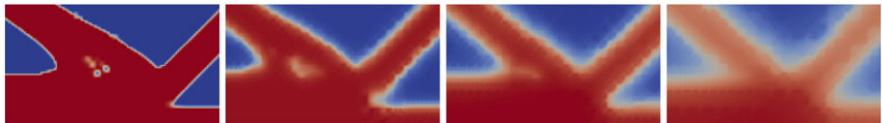


FIGURE 4 Close-up view of last row of results in Table 1. The results for $r = 0$ (far left) show multiple small holes emerging in the middle of solid material. These holes have been filled in with weak material when $r = 1.25$ (center left) and do not appear at all when $r = 2.5$ or $r = 5$ (center and far right)

initial design mesh element size. The zero-radius filter is also presented for comparison. In the cases of $r = 5.0$ and $r = 2.5$, the filter succeeds in preventing the appearance of the small holes visible in the finest mesh with $r = 0$. The filter with $r = 1.25$ is partially successful in that the location of the hole is still visible in the results, but the hole itself is filled in with weakened material. Figure 4 provides a close-up view of this part of the beam for each filter size.

Figure 5 shows the evolution of the design and analysis meshes for the $r = 0$ column in Table 1. The behavior of the adaptive refinement is typical of the test problems shown in this paper. The most refined cells are located near where the mesh refinement indicator (5) perceives a solid-to-void transition so the meshes themselves evolve to conform to the optimal material boundary. Table 2 shows the number of DOFs in each of these meshes along with the number of constrained DOFs, ie, the number of hanging nodes created by the adaptive refinement scheme. If global refinement was used instead of local refinement, the number of DOFs would increase by a factor of 4 with each refinement instead of the results in Table 2 showing less than a factor of 2.5 in each case. In addition, significant fractions of these DOFs are constrained because they lie on hanging nodes, further reducing the costs of analysis and design.

The main drawback of using the density filter is that it maintains a transition region of prescribed width regardless of the underlying mesh refinement. In Table 1, it is quite apparent that the transition region continues to shrink when $r = 0$ even after 4 local refinements. For larger filter sizes, the transition region appears to stop shrinking when the smallest elements become smaller than the filter radius. For example, in the case of $r = 5.0$, the transition region stops shrinking after 2 refinements because the smallest elements in the mesh are 2.5 mm wide, smaller than the filter radius. Note, however, that the compliance of the optimized structure continues to decrease because the accuracy of the finite element model improves as the mesh is refined.

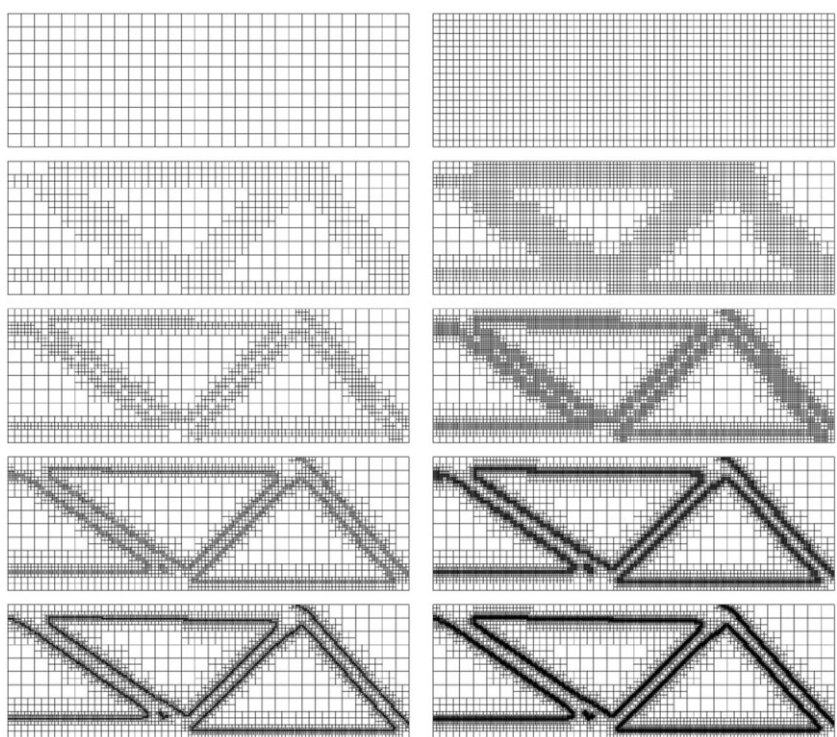


FIGURE 5 Evolution of design (left) and analysis (right) meshes for the Messerschmidt-Bolkow-Blohm problem for the case of $r = 0$ and an initial design mesh of 10×30 elements. The mesh evolution is driven by the desire to locate the optimal structural boundary

TABLE 2 Number of degrees of freedom (DOFs) for the meshes shown in Figure 5

Refinement level	No. of design mesh DOFs	No. of constrained design mesh DOFs	No. of analysis mesh DOFs	No. of constrained analysis mesh DOFs
0	341	0	2562	0
1	891	121 (13.6%)	6302	618 (9.8%)
2	2211	609 (27.5%)	14 996	2746 (18.3%)
3	4981	1539 (30.9%)	32 202	7468 (23.2%)
4	10 965	3799 (34.6%)	67 174	16 592 (24.7%)

The blurred boundary caused by the filter radius is especially obvious in Figure 4. However, this figure also shows the main positive attribute of the density filter when used together with adaptive mesh refinement. Because the filter prevents small holes from appearing when r is sufficiently large, the mesh does not need to be locally refined to precisely estimate the hole boundary. Where the mesh is not refined, mesh-dependent features cannot emerge. This is the key trade-off of using a density filter. While using the filter can prevent the mesh refinement from being too aggressive in searching for the boundaries around mesh-dependent features, it forces us to accept a transition region whose size is determined by the filter radius.

Table 3 shows the optimized topologies for 3 different filter sizes and 3 local refinements starting from a 20×60 element design mesh and 40×120 element analysis mesh. Compliance values are also included for reference. As with the results in Table 1, we see that compliance decreases as the mesh is refined and the size of the transition region is dictated by both the mesh refinement and the filter radius.

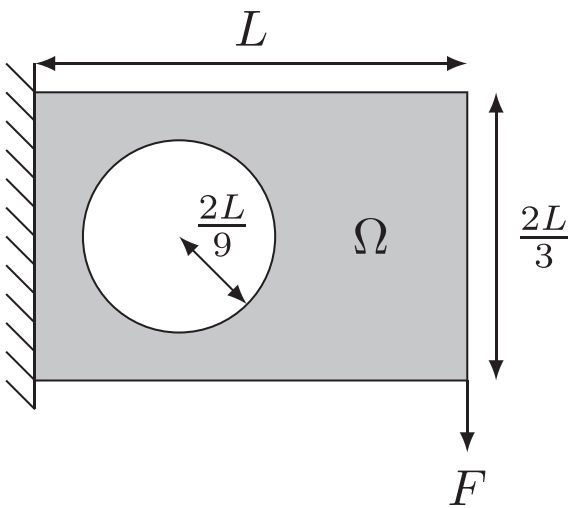
The most interesting result in this set of tests is for the case $r = 0$. Table 3 shows no holes or small structural members emerging anywhere within the structure. This is an ideal result because the optimized structure contains no topological features smaller than the elements of the initial mesh, yet it shows a precise optimal structural boundary after a few adaptive refinements. In contrast, the results of the same problem in Lambe and Czekanski¹⁹ did show the emergence of small holes in the optimal structure as the mesh was refined. We believe this is the result of the filter causing the optimizer to take a different search path to find a different local optimum. The results using $r = 1.25$ in Table 3 do show a small hole emerging in the density field that is filled in by the action of the filter.

TABLE 3 Messerschmidt-Bolkow-Blohm beam example with 20×60 element starting mesh

$r = 0$	$r = 1.25$	$r = 2.5$
$C = 50.069$	$C = 54.314$	$C = 63.991$
$C = 44.101$	$C = 48.051$	$C = 55.980$
$C = 42.056^*$	$C = 46.189$	$C = 53.199$
$C = 41.108^*$	$C = 45.392$	$C = 52.107$

Note. Compliance values are in N·mm. Results are ordered top-to-bottom, coarsest design mesh to finest.

*This indicates that the desired optimality tolerance could not be achieved for that problem.

**FIGURE 6** The cantilever beam problem geometry

5.2 | Cantilever beam problem

The second example is a cantilever beam with an enforced circular hole in the domain. Figure 6 depicts the geometry. We take $F = 150$ N and $L = 150$ mm in this example. Figure 7 shows 2 initial design meshes for this example. We have chosen to use a conforming design mesh in this example to demonstrate the robustness of the algorithm in the presence of irregular mesh topology. An alternative approach would be to embed the design domain in a rectangular design mesh and only use a conforming mesh for the structural analysis. However, this approach requires separate refinement indicators for the 2 meshes.

Table 4 shows refinement results for the 80-element initial design mesh with 3 different filter radii. In all cases, the structural boundary is progressively smoothed out despite being poorly aligned with the initial mesh. As with the MBB beam examples, small structural features emerge as the mesh is refined if the filter radius is too small. This example also shows 2 different locally optimal designs at the finest mesh refinement depending on the filter radius.

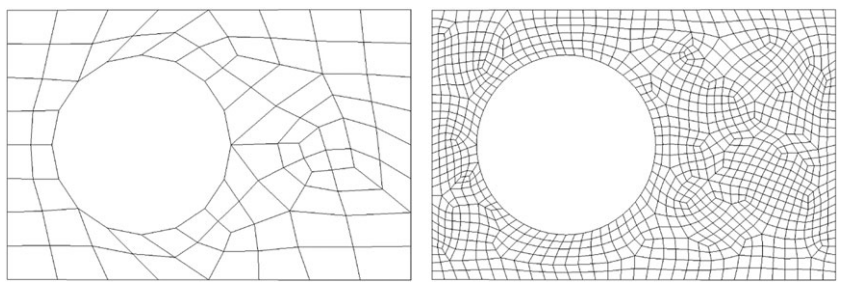
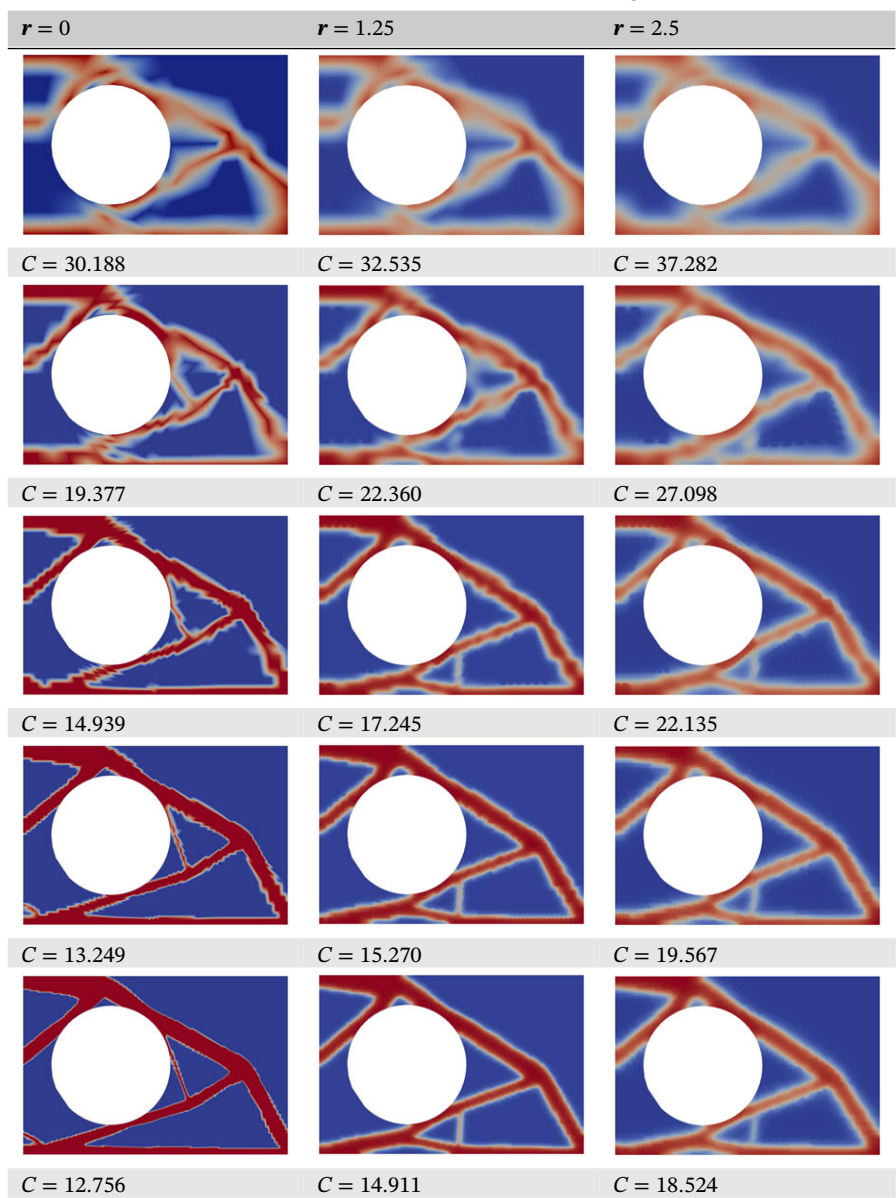


FIGURE 7 Coarse and fine initial design meshes for the cantilever beam problem. The coarse mesh contains 80 elements while the fine mesh contains 1044 elements

TABLE 4 Cantilever beam example with an 80-element starting mesh



Note. Compliance values are in N-mm. Results are ordered top-to-bottom, coarsest design mesh to finest.

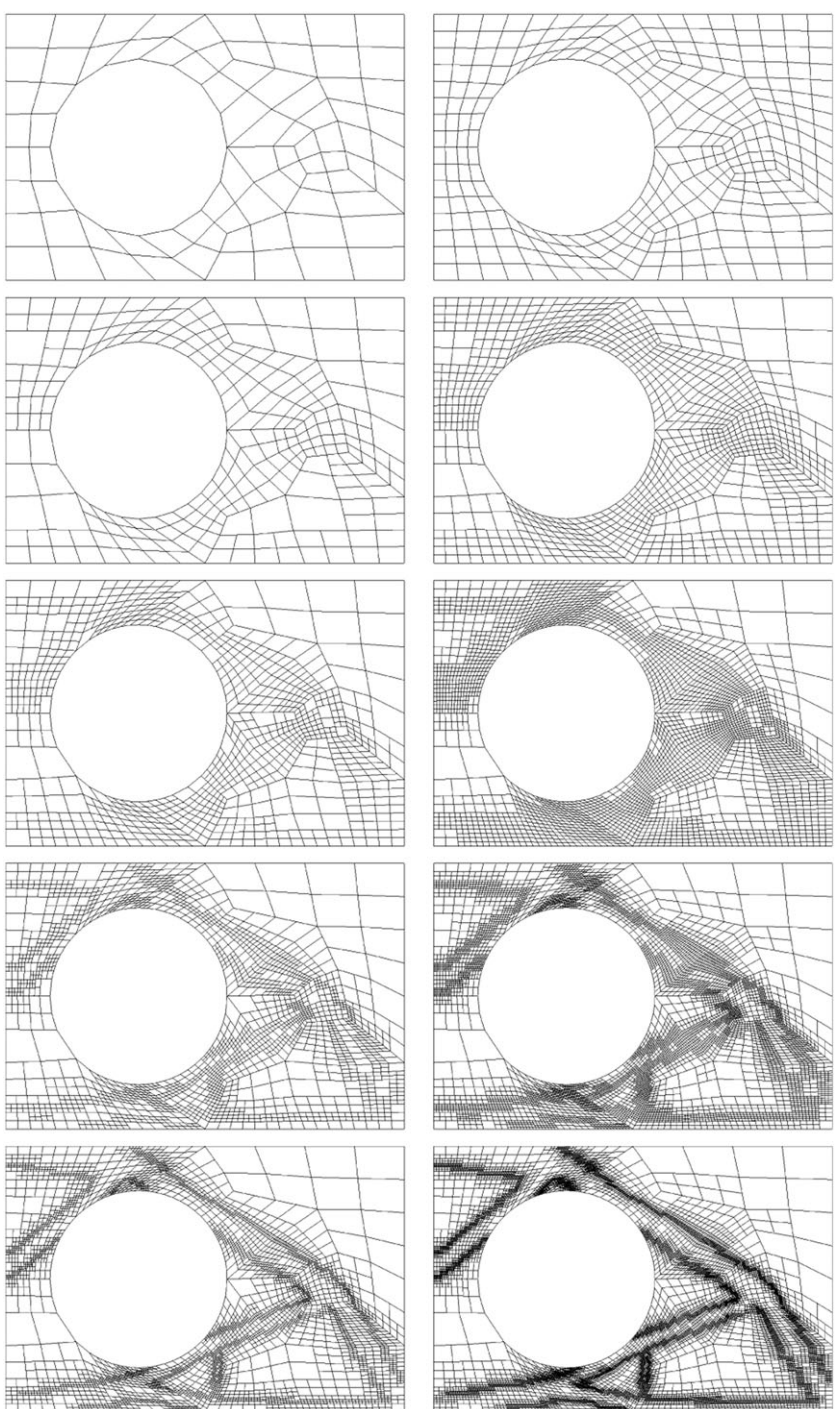
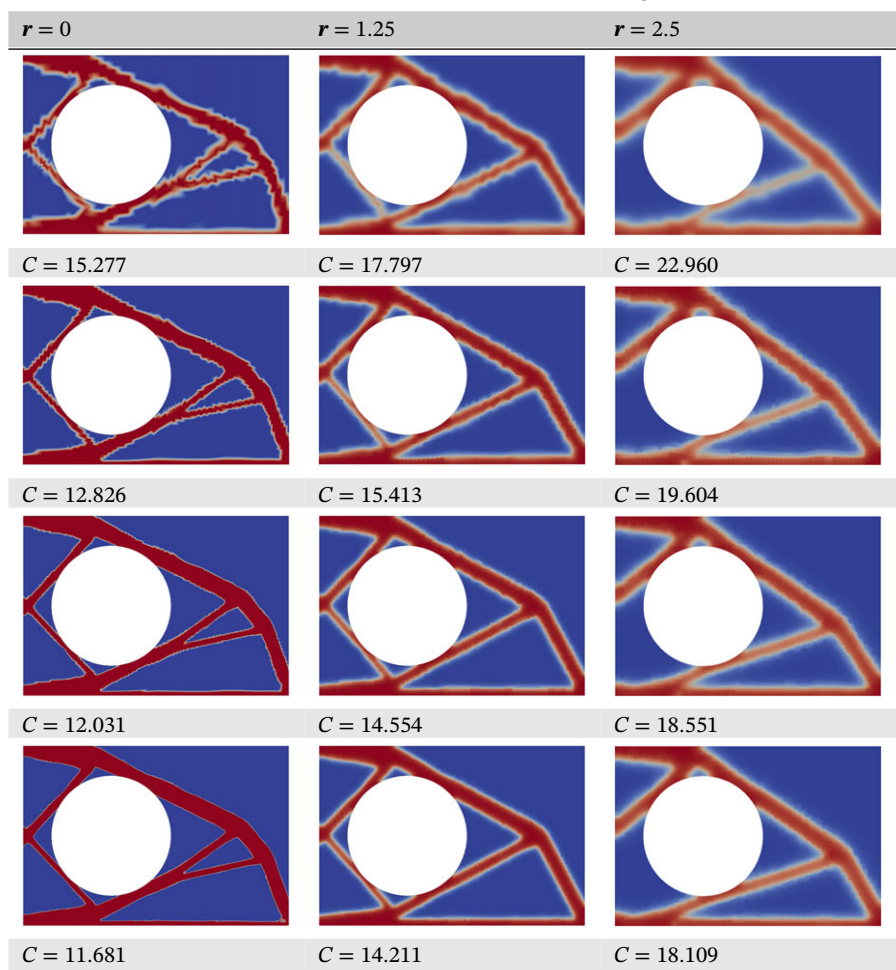


FIGURE 8 Evolution of design (left) and analysis (right) meshes for the cantilever beam problem with an 80-element initial design mesh for the case of $r = 1.25$. Even when the density filter has finite radius and the mesh conforms to the domain shape, the adaptive refinement scheme acts to isolate the optimal material boundary

Figure 8 shows the mesh evolution of this problem for the case $r = 1.25$. Table 5 shows the number of DOFs and hanging node constraints in each mesh. These results confirm our observations for the meshes found on the MBB beam problem: The local refinement acts to increase the number of elements near the optimal structural boundary but keep the total analysis and design DOFs lower than we would expect using global refinement. Once again, the fraction of constrained DOFs in both meshes increases with every refinement. Since we obtain similar results for both rectilinear and conforming meshes both with and without using the density filter, these behaviors are likely shared with all meshes generated by our method.

TABLE 5 Number of degrees of freedom (DOFs) for the meshes shown in Figure 8

Refinement level	No. of design mesh DOFs	No. of constrained design Mesh DOFs	No. of analysis mesh DOFs	No. of constrained analysis mesh DOFs
0	104	0	736	0
1	300	29 (9.7%)	2128	138 (6.5%)
2	895	133 (14.9%)	6454	598 (9.3%)
3	2222	587 (26.4%)	15 218	2696 (17.7%)
4	5148	1588 (30.8%)	33 314	7306 (21.9%)

TABLE 6 Cantilever beam example with a 1044-element starting mesh

Note. Compliance values are in N-mm. Results are ordered top-to-bottom, coarsest design mesh to finest.

Table 6 shows refinement results for the 1044-element initial mesh. This finer mesh allows the optimal design to incorporate smaller members than those found in the first row of Table 4. The action of the filter to impose a minimum length scale on the optimal structural is especially clear in this example. All 3 choices of filter radius result in different yet locally optimal topologies.

Comparing Table 6 with 4, we also observe that starting with a finer mesh seems to prevent the emergence of mesh-dependent features as the mesh is refined. This follows the MBB beam problem results in Table 3 and would seem to confirm an observation by Rahmatalla and Swan that the “islanding” phenomenon is mitigated by using a more fine initial mesh.²⁰ The reason that these numerical artifacts are avoided on fine initial meshes is not clear at this time.

5.3 | Further examples with complex geometry

To further demonstrate the versatility of this approach, 2 more examples with a geometrically complicated design domain are solved. Both are based on problems solved by Talischi et al.²⁷ Figure 9 shows the geometry of the “wrench” problem

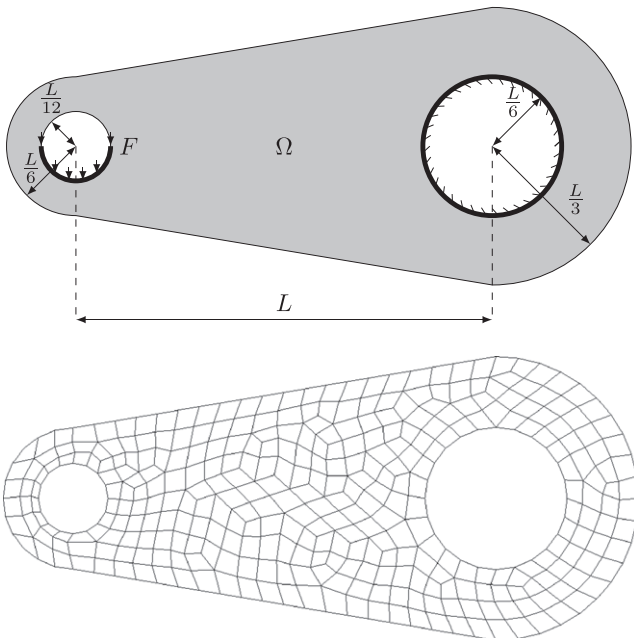


FIGURE 9 Geometry and initial design mesh for the wrench problem. The mesh contains 335 elements

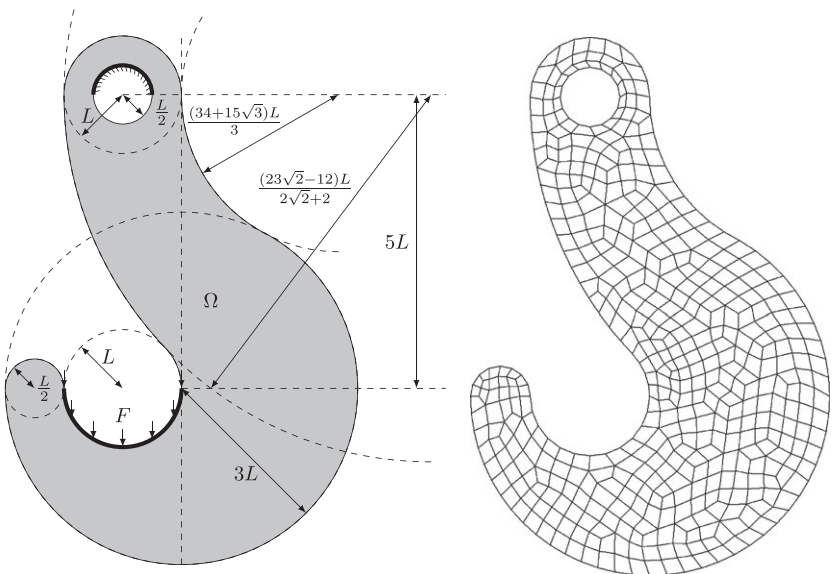
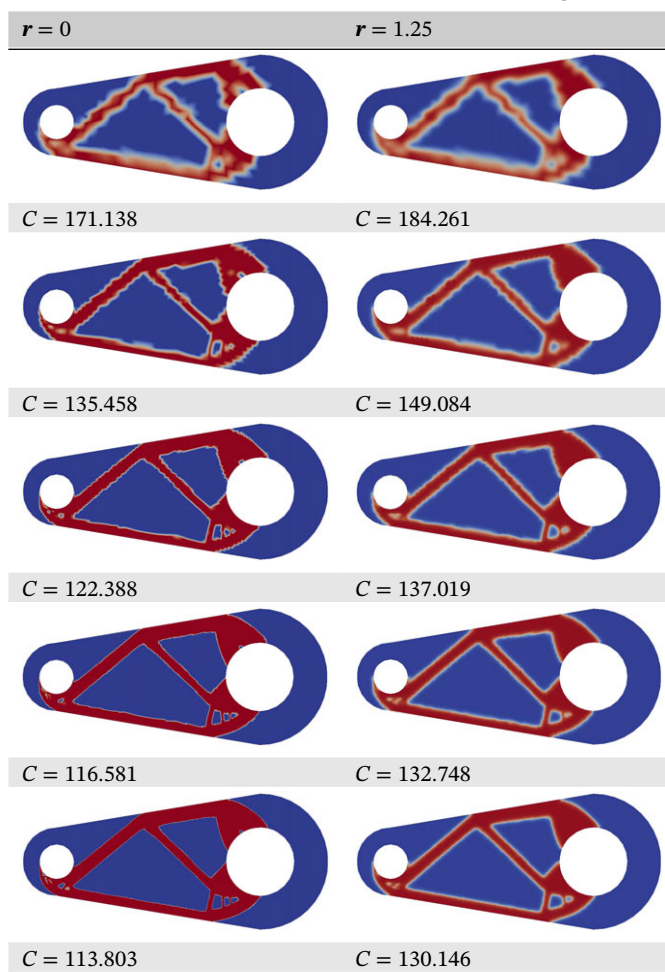


FIGURE 10 Geometry and initial design mesh for the hook problem. The mesh contains 462 elements

while Figure 10 depicts the “hook” problem. Both figures also include the initial design meshes. In both problems, the distributed force F is 10 N/mm. The characteristic length scale L is 180 mm for the wrench problem and 30 mm for the hook problem.

Table 7 shows the results of the wrench problem with filters $r = 0$ and $r = 1.25$. The results follow the pattern established with the 2 previous example problems, with the optimal compliance decreasing as the mesh is refined and the filter maintaining a transition region of prescribed length as the mesh is refined. One new feature of this example is that the load is distributed, rather than a point load. In the region near this distributed load, a number of small holes emerge as the mesh is refined. Figure 11 shows a close-up of this phenomenon. Use of the density filter is essential to smooth out these features in the final design.

TABLE 7 Wrench example with an 335-element starting mesh

Note. Compliance values are in N-mm. Results are ordered top-to-bottom, coarsest design mesh to finest.

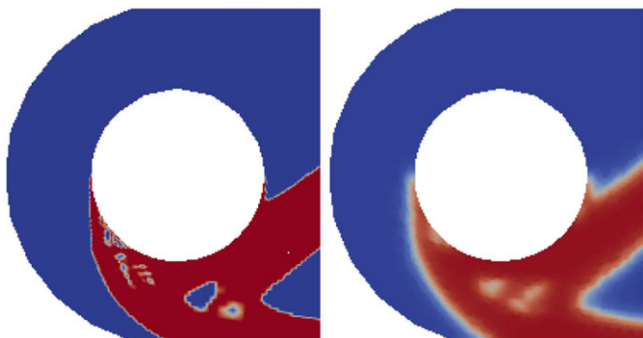
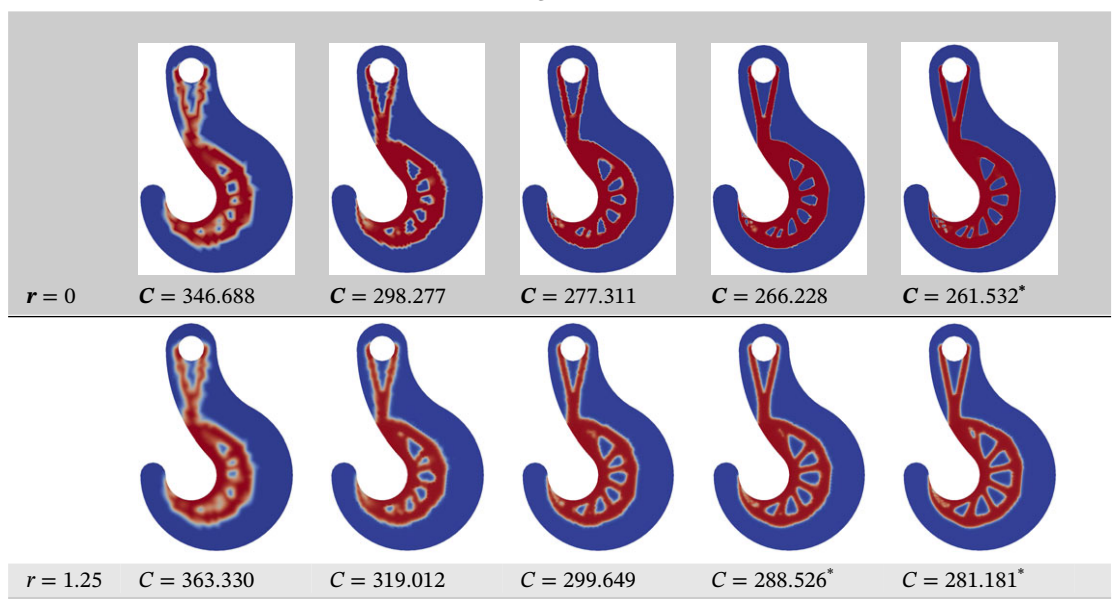


FIGURE 11 Close-up view of last row of results in Table 7. The results without the filter (left) show a number of small holes emerging near the distributed load location. These holes have been filled in when the filter is used (right)

Table 8 shows results for the hook problem with filters $r = 0$ and $r = 1.25$. As with the wrench example, a number of small holes appear near the distributed load when the zero-length filter is used. Figure 12 gives a close-up view of this part of the structure. One unusual observation with this set of results is that the large holes in the main body of the structure seem to be growing with each mesh refinement. At the same time, the outer boundary of the optimal hook seems to be moving outward toward the design domain boundary. Table 8 notes that IPOPT had difficulty reaching the optimality tolerance in the most refined examples regardless of filter length, so the cause may be a mesh quality issue.

TABLE 8 Hook example with an 462-element starting mesh

Note. Compliance values are in N·mm. Results are ordered left-to-right, coarsest design mesh to finest.

*This indicates that the desired optimality tolerance could not be achieved for that problem

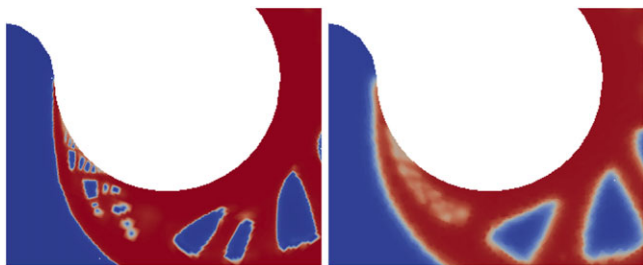


FIGURE 12 Close-up view of last column of results in Table 8. The results without the filter (left) show a number of small holes emerging near the distributed load location. These holes have been filled in when the filter is used (right)

6 | CONCLUSIONS

We have developed a density-based topology optimization method combining a continuous parametrization of the density field with adaptive mesh refinement to estimate the optimal structural boundary. An important contribution of this work is the use of different design and analysis meshes to prevent isolated islands of material from appearing in the optimal topologies. We also used a Helmholtz-type density filter to prevent the appearance of undesirable small features as the design and analysis meshes are refined. Unlike similar works using this density filter, we used filter radii that were smaller than the smallest elements in the initial design mesh so that the filter's effect was strongest on refined meshes. Finally, we showed how the method may be used to solve problems defined on geometrically complex domains.

We pursued the goal of accurate material boundary estimation in density-based topology optimization through adaptive mesh refinement. While our results showed some progress toward this goal, the need to use a density filter to prevent the emergence of mesh-dependent features is a major limitation. The filter radius not only imposes a transition region of fixed size on the optimized topology but also changes the optimal design in some instances. A compromise solution may be to reduce the filter radius at the same time as refining the mesh. This would allow the boundary to gradually sharpen but allow the filter to continue to suppress structural features smaller than the current mesh size. Another potential solution is to use a location-dependent filter, so that less filtering is done near the boundary once it is identified. This could be done under the Helmholtz filter framework by making r a function of location instead of a fixed value. Working around this compromise imposed by the density filter is the main difficulty to overcome to make the method practical to use.

ACKNOWLEDGMENTS

The authors would like to thank Michael Ihilchik for his assistance in setting up the hook and wrench problems shown in this work.

ORCID

Andrew B. Lambe  <http://orcid.org/0000-0003-1817-4271>

REFERENCES

1. Deaton JD, Grandhi RV. A survey of structural and multidisciplinary continuum topology optimization: post 2000. *Struct Multidisc Optim*. 2014;49(1):1-38en. <https://doi.org/10.1007/s00158-013-0956-z>
2. Bourdin B. Filters in topology optimization. *Int J Numer Methods Eng*. 2001;50(9):2143-2158.
3. Sigmund O, Petersson J. Numerical instabilities in topology optimization: a survey on procedures dealing with checkerboards, mesh-dependencies, and local minima. *Struct Multidisc Optim*. 1998;16(1):68-75.
4. Lazarov BS, Sigmund O. Filters in topology optimization based on Helmholtz-type differential equations. *Int J Numer Methods Eng*. 2011;86:765-781.
5. Guest JK, Prévost JH, Belytschko T. Achieving minimum length scale in topology optimization using nodal design variables and projection functions. *Int J Numer Methods Eng*. 2004;61:238-254.
6. Matsui K, Terada K. Continuous approximation of material distribution for topology optimization. *Int J Numer Methods Eng*. 2004;59(14):1925-1944. <https://doi.org/10.1002/nme.945>
7. Nguyen TH, Paulino GH, Song J, Le CH. A computational paradigm for multiresolution topology optimization (MTOP). *Struct Multidisc Optim*. 2010;41:525-539.
8. Kang Z, Wang Y. Structural topology optimization based on non-local Shepard interpolation of density field. *Comput Meth Appl Mech Eng*. 2011;200:3515-3525.
9. Qian X. Topology optimization in B-spline space. *Comput Meth Appl Mech Eng*. 2013;265:15-35. <https://doi.org/10.1016/j.cma.2013.06.001>
10. Paulino GH, Le CH. A modified Q4/Q4 element for topology optimization. *Struct Multidisc Optim*. 2009;37(3):255-264. <https://doi.org/10.1007/s00158-008-0228-5>
11. van Dijk NP, Maute K, Langelaar M, van Keulen F. Level-set methods for structural topology optimization: a review. *Struct Multidisc Optim*. 2013;48(3):437-472.
12. Guest JK, Asadpoure A, Ha SH. Eliminating beta-continuation from Heaviside projection and density filter algorithms. *Struct Multidisc Optim*. 2011;44:443-453.
13. Maute K, Ramm E. Adaptive topology optimization. *Struct Optim*. 1995;10(2):100-112. <https://doi.org/10.1016/10.1007/BF01743537>
14. Costa Jr JCA, Alves MK. Layout optimization with h-adaptivity of structures. *Int J Numer Methods Eng*. 2003;58(1):83-102. <https://doi.org/10.1002/nme.759>
15. Stainko R. An adaptive multilevel approach to the minimal compliance problem in topology optimization. *Commun Numer Methods Eng*. 2005;22(2):109-118. <https://doi.org/10.1002/cnm.800>
16. Bruggi M, Verani M. A fully adaptive topology optimization algorithm with goal-oriented error control. *Computers & Structures*. 2011;89(15-16):1481-1493. <https://doi.org/10.1016/j.compstruc.2011.05.003>
17. Guest JK, Smith Genut LC. Reducing dimensionality in topology optimization using adaptive design variable fields. *Int J Numer Methods Eng*. 2009;81:1019-1045. <http://doi.org/10.1002/nme.2724>
18. Wang Y, Kang Z, He Q. Adaptive topology optimization with independent error control for separated displacement and density fields. *Computers & Structures*. 2014;135:50-61. <https://doi.org/10.1016/j.compstruc.2014.01.008>
19. Lambe AB, Czekanski A. Adaptive topology optimization using a continuous approximation of material distribution. In: ASME International Mechanical Engineering Congress and Exposition. Phoenix, AZ; 2016. <https://doi.org/10.1115/IMECE2016-65537>
20. Rahmatalla S, Swan C. A Q4/Q4 continuum structural topology optimization implementation. *Struct Multidisc Optim*. 2004;27(1-2):130-135. <https://doi.org/10.1007/s00158-003-0365-9>
21. Jog CS, Haber RB. Stability of finite element models for distributed-parameter optimization and topology design. *Comput Meth Appl Mech Eng*. 1996;130:203-226.
22. Zhou M, Rozvany GIN. The COC algorithm, part ii: topological, geometrical, and generalized shape optimization. *Comput Meth Appl Mech Eng*. 1991;89:309-336.
23. Bangerth W, Hartmann R, Kanschat G. deal.II—a general-purpose object-oriented finite-element library. *ACM Trans Math Softw*. 2007;33:24/1-24/27.
24. Geuzaine C, Remacle JF. Gmsh: a three-dimensional finite element mesh generator with built-in pre- and post-processing facilities. *Int J Numer Methods Eng*. 2009;79(11):1309-1331.
25. Wächter A, Biegler L. On the implementation of a primal-dual interior point filter line search algorithm for large-scale nonlinear programming. *Math Program*. 2006;106:25-57.

26. Holmberg E, Torstensfelt B, Klarbring A. Stress constrained topology optimization. *Struct Multidisc Optim.* 2013;48(1):33-47. <http://doi.org/10.1007/s00158-012-0880-7>
27. Talischi C, Paulino GH, Pereira A, Menezes IFM. Polytop: a Matlab implementation of a general topology optimization framework using unstructured polygonal finite element meshes. *Struct Multidisc Optim.* 2012;45(3):329-357.

How to cite this article: Lambe AB, Czekanski A. Topology optimization using a continuous density field and adaptive mesh refinement. *Int J Numer Meth Engng.* 2018;113:357–373. <https://doi.org/10.1002/nme.5617>